

SOME RESULTS FROM A STUDY OF $\pi^- p \rightarrow \rho^0 X^0$ AT 15 GEV/C*

D. W. G. S. LEITH

INTRODUCTION

I wish to report on some of our results from a wire spark chamber experiment at SLAC, studying the reaction $\pi^- p \rightarrow \rho^0 X^0$ for small momentum transfers at an incident momentum of 15 GeV/c. The results reported here are the work of the following people:

P. Baillon, F. Bulos, R. K. Carnegie, G. Fischer, E. E. Kluge,
D. W. G. S. Leith, H. L. Lynch, B. Ratcliff, B. Richter,
H. H. Williams, and S. H. Williams.

The experiment focussed on the opposite end of the momentum transfer scale than the spectacular electron scattering experiments at SLAC. They were using very large t , thus probing small distances within the nucleon, looking for signs of structure within the proton and neutron. Our experiment, on the other hand, was focussed at very small momentum transfers, looking at large distance, long range phenomena. Basically, we were probing the pion exchange structures and attempting to see the characteristic signature of the pion

* Work supported by the U.S. Atomic Energy Commission
(Presented at the 7th Rencontre de Moriond, Meribel-les-Allues,
France, March 5-17, 1972)

propagator at small t . It is surprising that, with the ideas of one-pion-exchange having been around for so many years, there have been no experimental observations of OPE-dominated reactions for $t < M_{\pi}^2$.

APPARATUS

The experimental arrangement is shown in Fig. 1. The incident π^- beam, of ~ 10 π 's per pulse at 180 pulses per second, has the momentum and angles of each particle measured by scintillation counter hodoscopes to an accuracy of $\pm 0.3\%$ and ± 0.5 mrad, respectively. The spectrometer consists of seven 2-gap wire spark chambers, 3 before and 4 after the analysing magnet. The magnet had a gap of (100 x 40) cms and was 120 cms long with a field strength of ~ 26 Kg meters. The inside surfaces of the magnet were covered with scintillation counters, which vetoed events in which particles smashed into the steel of the magnet.

The trigger was given by the XY hodoscope, in front of the target, in coincidence with two particles passing through the two large "picket fence" hodoscopes behind the analysing magnet. The target was surrounded by a scintillator-lead-scintillator sandwich counter which helped to identify the other particles produced in the reaction. This counter was not in the trigger logic as it would have introduced strong t -dependent biases.

The wire spark chambers, constructed of Al-Dacron cloth, were (1 x 1/2) m in area in front of the magnet and (1-1/2 x 1) m behind. These chambers were capable of operating at 180 pps with

multiple track efficiency, ($> 95\%$ for 8 tracks), and with good spatial accuracy, ($\leq \pm 1/2$ mm). The chambers were deadened in the region where the π^- beam passed through, by 4 cm diameter polyurethane plugs.

Finally, a large threshold Cerenkov hodoscope allowed selection of pions from heavier particles (K, p).

RAW DATA

In Fig. 2 the effective mass of all $\pi^+\pi^-$ events is plotted. The rho dominates the $(\pi^+\pi^-)$ mass spectrum, but the K_1^0 decays are also clearly seen, with the f^0 just appearing as a shoulder around 1250 MeV due to the fall-off in the high mass acceptance of the apparatus.

Selecting on the rho events, we now look at the missing mass spectrum, Fig. 3. The neutron, $N^*(1400)$ region, and $N^*(1700)$ region signals are present, above background. We may investigate the missing neutron signal further by use of the counter surrounding the target, as shown in Fig. 4. By demanding that no counts appear in the lead-scintillator counter, a very clean neutron peak is isolated, but there is also a $\sim 30\%$ loss of events. This loss comes from vetoing real neutron events in which neutron-proton knock-ons or δ -rays count in the target counter. Further, these losses are strong functions of the momentum transfer to the neutron and the π - π scattering angle -- both variables which we are attempting to study. We do not select events in this way. The intermediate histogram in Fig. 4 is the missing mass spectrum to rho events, where the target counter vetos events in which two of the eight

scintillators have fired. (The likelihood of real $\pi^+\pi^-n$ events producing such a signal is very small.)

In Fig. 5, the $\pi^+\pi^-$ mass spectrum is shown for events recoiling against a neutron. Again the rho dominates the picture, with $K_1^0 \rightarrow \pi^+\pi^-$ still breaking through, (the missing mass selection does not exclude Λ , Σ recoils) and the f^0 region becoming slightly more credible. About 40% of the data shown in this plot was taken under "high resolution" conditions and has been used for the small $t \pi^-p \rightarrow \rho^0n$ studies, and the ρ - ω interference study described elsewhere. (2)

The mass resolution and absolute calibration of the mass scale was studied using the $K_1^0 \rightarrow \pi^+\pi^-$ decays which we have observed in the $\pi^+\pi^-$ mass plots. In Fig. 6 these events are shown in 2 MeV mass bins. These events were selected such that the K_1^0 decayed within the target volume, so that the multiple scattering effects in hydrogen were included. The K^0 peak was then fitted to a gaussian resolution function with a linear background term.

The K^0 mass and mass resolution of the system is given by

$$M(K^0) = 497.4 \pm 1.0 \text{ MeV}$$

$$\sigma(K^0) = 6.5 \pm 1.0 \text{ MeV}$$

where the errors include conservative estimates of the systematic effects. This compares well with the accepted K^0 mass of $(497.79 \pm .15) \text{ MeV}$.

There were sufficient $K^0 \rightarrow 2\pi$ decays that K^0 mass distributions could be studied for blocks of 5-10 runs, to check for systematic shifts in the mass scale during the run.

The mass resolution for the rho events will be somewhat larger, due to the greater Q-value, and is estimated to be $\sigma(\rho) \sim 8$ MeV.

DECAY DISTRIBUTIONS

The decay angular distributions for the $\pi^-p \rightarrow \rho^0 n$ events were determined as a function of momentum transfer, t , by fitting to the following forms.

$$\omega(\theta, \phi) = W(\theta, \phi)E(\theta, \phi) \text{ where}$$

$$W(\theta, \phi) = \frac{1}{4\pi} \left[1 + (\rho_{00} - \rho_{11})(3 \cos^2 \theta - 1) + 2\sqrt{3} \operatorname{Re}(\rho_{0S}) \cos \theta \right. \\ \left. - 3\sqrt{2} \operatorname{Re}(\rho_{10}) \sin 2\theta \cos \phi - 2\sqrt{6} \operatorname{Re}(\rho_{1S}) \sin \theta \cos \phi \right. \\ \left. - 3\rho_{1-1} \sin^2 \theta \cos 2\phi \right]$$

$$\rho_{00} + 2\rho_{11} + \rho_{00}^S = 1.$$

where $\omega(\theta, \phi)$ is the angular distribution for S, P waves only, and $E(\theta, \phi)$ is the detection efficiency.

θ, ϕ are the polar and azimuthal angle of the π^- in the ρ rest frame.

ρ_{ij} are normalised by $\rho_{00} + 2\rho_{11} + \rho_{00}^S = 1$.

The ρ region was defined as $0.665 \leq M_{\pi^+\pi^-} \leq 0.865$ GeV.

$E(\theta, \phi)$ was evaluated using a Monte Carlo program.

The density matrix elements are shown in Fig. 7, for the helicity frame, and in Fig. 8 for the Gottfried-Jackson frame. The density matrix elements show considerable structure for small t , especially $\rho_{00} - \rho_{11}$ which exhibits a very pronounced dip for $t < \frac{1}{3}M_\pi^2$.

This is the turnover expected from the pion exchange propagator, but appearing at even smaller t values than expected. This turnover is present in both coordinate systems. There is also interesting structure in $\text{Re } \rho_{10}^H$ and $\text{Re } \rho_{1S}^H$, both of which have negative values for $0 \leq t \leq M_\pi^2$ and then cross over through zero at $t = M_\pi^2$, and have positive values for larger t .

We have mentioned above that it is not possible to isolate out the longitudinal and transverse p-wave components and the s-wave component from this experiment alone. However, there are several methods by which we can estimate the s-wave contribution to the $\pi^+\pi^-n$ final state.

The first of these methods is to apply the Schwartz inequalities to the helicity amplitudes, which then yields the limits on ρ_{11}^H shown in Fig. 9. The points represent the upper and lower limits while the error bars indicate the errors on the limits resulting from propagation of the errors on the measured density matrix element, ρ_{ij} . It is interesting to note that the limits determine ρ_{11}^H rather well for $t > M_\pi^2$, but below that the limits diverge strongly.

Other estimates for the s-wave background may be obtained from study of the $\pi^+\pi^-$ mass plot, assuming that only s-, and p-waves contribute to the $\pi^+\pi^-$ amplitude for $M_{\pi\pi} < 900$ MeV from study of the data on $\pi^-p \rightarrow \pi^0\pi^0n$, from OPE fits to the $\pi^0\pi^0$ data, and from OPEA fits to the present $\pi^+\pi^-n$ data. All of these methods give the same total s-wave contribution of (10-12)%, with a behavior in t given well by $|t| / (t-\mu^2)^2 e^{7t}$. For a more detailed discussion of the treatment of the s-wave see reference 1.

The differential cross section, together with the cross section for transversely polarised rho production in the helicity frame is shown in Fig. 10. The longitudinal rho and transverse rho cross sections for the Jackson system are shown in Fig. 11.

It is interesting to see the turnover in the differential cross section, especially the deep turnover in the longitudinal cross section expected from the pion propagator. However, even more striking is the very sharp forward spike in $\rho_{11}^H d\sigma/dt$. This sharp structure is not expected in simple pion exchange, but is expected only if absorption is present. The existence of this forward rise may be interpreted as strong qualitative confirmation of the vector dominance model.⁽²⁾

In Fig. 11, the longitudinal cross section shows a dip, but the transverse cross section (in Jackson system) is consistent with no structure, as expected since in this frame the pion exchange cannot contribute to non-zero helicity states.⁽³⁾

ONE PION EXCHANGE MODELS

The above data -- large value for $(\rho_{00} - \rho_{11})$, $\rho_{1-1}^{GJ} \sim 0$, ρ_{ij} and $d\sigma/dt$ structure for $t < M_\pi^2$ -- show strong indications of one pion exchange being a dominant process for the reaction $\pi^- p \rightarrow \pi^+ \pi^- n$. However, the fact that $(\rho_{00}^{GJ} - \rho_{11}^{GJ}) \neq 1$, that ρ_{11}^H shows a strong peak for $t < M_\pi^2$ and that $2\rho_{11}^H d\sigma/dt$ shows a sharp forward peak near $t = 0$ are all strong indicators of absorptive effects. Below, we list a number of predictions of one pion exchange with absorption-OPEA models, for the small t region ($-t < M_\pi^2$) first given by M. Ross et al.⁽⁴⁾ Prior to this

experiment they had not been directly verified.

1. ρ_{11}^{GJ} and ρ_{11}^H $d\sigma/dt$ should have sharp forward peaks.
2. ρ_{00}^{GJ} and $d\sigma/dt$ should have forward turnovers.
3. ρ_{11}^{GJ} $d\sigma/dt$ should have no structure.
4. $\rho_{1-1}^H / \rho_{11}^H$ should behave like $-t/M_\pi^2$.
5. $\rho_{1-1}^{GJ} \approx 0$.

These qualitative features of OPEA are all confirmed in our experiment, as shown in Fig. 12.

A more quantitative approach has also proved to be quite successful. Results have already been published for $\pi^- p \rightarrow \pi^+ \pi^- n$ (5) and I will present preliminary results for $\pi^- p \rightarrow \pi^+ \pi^- \Delta^{+0+}$ -- final results will be available shortly.

Although it is generally accepted that absorptive corrections are important, there is no unique method of applying them. Kane et al. (6) suggested a simplified version (of the cumbersome many parameter generalised OPEA) in which the absorptive corrections are performed directly on the helicity amplitudes without the necessity of partial wave expansion. P. K. Williams (7) further simplified the model down to four parameters by making additional constraints on the model.

For convenience we use the formulation of the OPEA model given by Williams and described in some detail in reference 5. Basically the model assumes:

1. That helicity flip amplitudes will dominate at high s for $\pi^+ \pi^- n$ and non-flip for $\pi \pi \Delta$.

2. For small t , the t dependence is given by the minimum t dependence to give angular momentum conservation along the beam axis.
3. Absorption is introduced as helicity-independent collimating factor -- $e^{A(t-\mu^2)}$.
4. At the pion pole only π -exchange will survive and so there will be no natural parity exchange (i.e. $(\rho_{11} + \rho_{1-1}) = 0$). (This implies constraints between the two transverse amplitudes, both in magnitude and phase.)
5. That relationships between the longitudinal and transverse amplitudes at the pion pole give

$$\frac{\rho_{00}}{2\rho_{11}} = - \frac{M_{\pi\pi}^2}{4\mu^2} .$$

With these assumptions applied to the scattering amplitudes the only unknown quantities, at the pole, are the relative magnitude of the s-wave and p-wave, the relative s-p phase, the overall normalisation, and the parameter A which is related to the slope of the differential cross section.

This model was applied to the following three reactions independently --

$$\left. \begin{array}{l} \pi^- p \rightarrow \pi^+ \pi^- n \\ \rightarrow \pi^+ \pi^- \Delta^0 \\ \pi^+ p \rightarrow \pi^+ \pi^- \Delta^{++} \end{array} \right\} 0.665 \leq M_{\pi\pi} \leq 0.865 \text{ GeV},$$

and the results are shown in Figs. 13, 14, and 15. The fitting is limited to small t values, as the above assumptions are only valid

in this region. The model clearly fits the data rather well in all three cases.

I don't want to go into the details of the particular model fits, but rather discuss some qualitative features.

In Fig. 13 the data are well described by the model, including the sharp structure for $-t < M_\pi^2$. The model required $\approx 10\%$ of non-flip amplitude to fit, and this was taken to be the effect of $\pi^+\pi^-\Delta^0$ events included in the neutron missing mass cut. (It appears that this 10% fraction is too large to be explained by background in the missing mass cuts, and probably indicates some ($\sim 5\%$) real non-flip contribution to $\pi^+\pi^-n$.)

The Figs. 14 and 15 are also well fit, this time with a non-flip amplitude. The SU_2 relationships between the amplitudes found in the fit for these two Δ processes are well satisfied.

It is impressive that such a simple model should fit all the data from these three reactions so economically, and surely strongly supports the need to take account of absorptive effects in studying OPE processes.

π - π SCATTERING

Finally, we briefly examine our data from the point of view of studying π - π scattering. We have shown above that absorptive effects are important, and that $2\rho_{11}^H d\sigma/dt$ has a sharp peak for $t \sim 0$. Therefore, in extrapolating the physical region cross sections to the pion pole we should not constrain the cross section to vanish at $t = 0$, as in classical Chew-Low extrapolations. Also in our favor are the high energy of the experiment, and the very

small t values at which we have data.

We use the following data:

$$\begin{array}{ll} \pi^- p \rightarrow \pi^+ \pi^- n & 17,000 \text{ events} \\ \rightarrow \pi^+ \pi^- X^0 & 50,000 \text{ events (inclusive of} \\ & \text{the } \pi^+ \pi^- n \text{).} \end{array}$$

where $M(X^0) \leq 1.39 \text{ GeV}$, and where the $\pi^+ \pi^- n$ data was used for both extrapolated angular distributions and for the absolute cross section, while the $\pi^+ \pi^- X$ was used to give the shape of the angular distribution, only. The extrapolation was performed with a polynomial in t , and using the conformal mapping technique used by Baton et al. (8,9) The latter technique was found to be more sensitive and was used in the following analysis.

The data was divided into nine 50 MeV mass intervals from 525 MeV to 975 MeV and 13 t intervals for $-t < 0.3 \text{ GeV}/c^2$, including 5 t bins within the region $-t < M_\pi^2$.

The extrapolated differential cross sections are shown in Fig. 16 for each mass interval. The black points are the results of the phase shift analysis.

An energy independent phase shift analysis was performed for each of the nine mass intervals separately. We assumed that only s- and p-waves were important and that the $\pi\pi$ scattering was entirely elastic throughout this energy region. In addition, the I=2 phases were taken from Baton et al. (8) The results are shown in Fig. 17. Note that there are two solutions for the elastic $\pi\pi$ cross section, $\sigma_{\pi\pi}$ (Fig. 17a), and for the p-wave phase shift, δ_1^1 (Fig. 17b), for those mass intervals for which we find two solutions in the s-wave; the up and down notation refers to the

corresponding s-wave solution. The results of Baton et al.⁽⁸⁾ for $\sigma_{\pi\pi}$ and δ_0^0 from their elastic phase shift analysis are shown for comparison.

The elastic $\pi\pi$ cross section does reach the unitary limit in the ρ region. Furthermore, although no particular mass dependence is imposed in this energy independent phase shift analysis, the p-wave result, δ_1^1 , is well represented by a Breit Wigner shape including centrifugal barriers. The parameters found are $M = 761 \pm 5$ MeV and $\Gamma = 108 \pm 20$ MeV.

We obtain a unique solution for the $I = 0$ s-wave phase shift for dipion masses below the ρ meson. A similar result for δ_0^0 in this region was found in the analysis of Baton et al.⁽⁸⁾ Above the ρ , the well-known up-down ambiguity persists for the three mass bins 800 through 900 MeV, again in good agreement with the results of Baton et al., shown in Fig. 17c; however, for the 950 MeV bin we find just a single solution.

It is of interest to examine the nature of the ambiguity in more detail. Fig. 18 displays the χ^2 obtained for each mass interval when δ_0^0 is fixed and the p-wave refitted. It should be noted that although each of the bins 800 through 900 MeV has a minimum solution, the difference in χ^2 is no longer sufficient to exclude the possibility of the other solution. Rather, in this region, one has a relatively broad valley in χ^2 space. The two branches for the δ_0^0 solutions would not appear to be as distinct as the traditional up-down notation implies and the possibility must be considered that the s-wave may cross 90° at a mass substantially higher than the mass range 700-750 MeV which is

customarily assumed. Indeed, the data on $\pi^- p \rightarrow \pi^0 \pi^0 n$ implies that the s-wave phase shift remains near 90° through the ρ region,⁽¹⁰⁾ which, taken with Fig. 17, would then imply that δ_0^0 cross 90° in the vicinity of 900-950 MeV, and be changing rapidly just below $\overline{K\overline{K}}$ threshold. Such a behavior is in accord with recent data on $\pi^+ p \rightarrow \pi^+ \pi^- \Delta^{++}$,⁽¹¹⁾ where rapid variations in the s-wave amplitude in this mass region were reported.

To summarize, we have performed an unconstrained Chew Low extrapolation of our data on $\pi^- p \rightarrow \pi^+ \pi^- X^0$ and determined the differential cross section for $\pi\pi$ scattering. An energy independent phase shift analysis finds that the elastic $\pi\pi$ cross section does reach the unitary limit at the ρ and yields a unique solution for the $I = 0$ s-wave phase shift below the ρ . While the precise behavior of δ_0^0 above the ρ remains an open question, arguments are presented for the phase shift crossing 90° at higher masses than conventionally accepted, viz. ~ 950 MeV. It is important to investigate this possibility further by extending systematic $\pi\pi$ phase shift studies to higher masses. This requires that D-wave effects and inelasticity be included, and therefore requires very high statistic experiments.

CONCLUSIONS

We have performed a fairly high statistics experiment at high s and for small t, and have indeed found characteristic signs of pion exchange for $t \lesssim M_\pi^2$. A study of the density matrix elements and cross sections has shown strong evidence for the existence of absorptive corrections. A simplified version of OPEA

was applied to the data for $\pi\pi n$ and $\pi\pi\Delta$ with surprisingly good results, again strongly supporting the presence of absorptive effects in the OPE process. Finally the same data was used to study π - π scattering at the pion pole and a useful set of phase shifts were obtained. Indications for new trends in the s-wave phase shift were discussed.

REFERENCES

1. H. H. Williams, Stanford Doctoral Dissertation, Report No. SLAC-142; F. Bulos, et al., Phys. Rev. Letters 26, 1453 (1971).
2. B. Ratcliff, Stanford Doctoral Dissertation, Report No. SLAC-141; F. Bulos et al., Phys. Rev. Letters 26, 1457 (1971).
3. Y. Avni and H. Harari, Phys. Rev. Letters 23, 262 (1969).
4. M. Ross et al., Nuclear Physics B23, 269 (1970).
5. P. Baillon et al., Phys. Letters 35B 453 (1971);
H. H. Williams, Stanford Doctoral Dissertation, Report No. SLAC-142.
6. G. Kane et al., Phys. Rev. 177, 2353 (1969).
7. P. K. Williams, Phys. Letters D1, 1312 (1970).
8. J. P. Baton et al., Phys. Rev. Letters 33B, 525 and 528 (1971).
9. R. E. Cutkosky and B. B. Deo, Phys. Rev. 174, 1859 (1968).
10. P. Sonderegger and C. Bonomy, Lund Conference, July 1969;
E. I. Shibata et al., Phys. Rev. Letters 25, 1227 (1970);
J. T. Carroll, Ph.D. Thesis, University of Wisconsin 1971,
(unpublished).
11. M. Alston-Garnjost et al., Phys. Letters 36B, 152 (1971).

FIGURE CAPTIONS

- Fig. 1 Schematic layout of the wire spark chamber spectrometer.
- Fig. 2 Effective $\pi^+\pi^-$ mass spectrum for the reaction $\pi^-p \rightarrow \pi^+\pi^-X^0$, at 15 GeV/c.
- Fig. 3 The missing mass spectrum for the reaction $\pi^-p \rightarrow \pi^+\pi^-X^0$, at 15 GeV/c, for $0.665 \leq M_{\pi\pi} \leq 0.865$ GeV.
- Fig. 4 The missing mass spectrum for the reaction $\pi^-p \rightarrow \pi^+\pi^-X^0$, at 15 GeV/c. The upper histogram is for all events; the single hatched histogram is for events in which two of the lead scintillator sandwich counters fired in coincidence; the double hatched histogram is for events in which no counts were recorded in the lead-scintillator counter around the target.
- Fig. 5 The effective $\pi^+\pi^-$ mass spectrum for the reaction $\pi^-p \rightarrow \pi^+\pi^-n$ at 15 GeV/c.
- Fig. 6 The effective $\pi^+\pi^-$ mass spectrum in the region of the K^0 .
- Fig. 7 The density matrix elements for rho decay, in the reaction $\pi^-p \rightarrow \rho^0n$, evaluated in the helicity frame.
- Fig. 8 The density matrix elements for rho decay, in the reaction $\pi^-p \rightarrow \rho^0n$, evaluated in the Gottfried-Jackson frame.
- Fig. 9 The upper and lower limits on ρ_{11}^H which are determined from the Schwartz inequalities on the helicity amplitudes and the requirement that the density matrix be positive definite. The errors on the limits result from the

propagation of the errors on the density matrix elements.

The curve is the calculated value of ρ_{11}^H obtained when the amount of s-wave is estimated from the $\pi^-p \rightarrow \pi^0\pi^0n$ data.

- Fig. 10 The differential cross section for $\pi^-p \rightarrow \rho^0n$, and the transverse cross section, $2\rho_{11} \frac{d\sigma}{dt}$, for $\pi^-p \rightarrow \pi^+\pi^-n$, where $0.665 < M_{\pi\pi} < 0.865$ GeV, both evaluated in the helicity frame.
- Fig. 11 The longitudinal and transverse differential cross sections in the Jackson frame for the reaction $\pi^-p \rightarrow \pi^+\pi^-n$, where $0.665 < M_{\pi^+\pi^-} < 0.865$ GeV.
- Fig. 12 Test for qualitative features of OPEA; (a) ρ_{00}^H , (b) ρ_{00}^{GJ} , (c) ρ_{11}^H , (d) ρ_{11}^{GJ} , (e) ρ_{1-1}^H/ρ_{11}^H -- the asymmetry, (f) ρ_{1-1}^{GJ} , (g) $\rho_{11}^H d\sigma/dt$, and (h) $\rho_{11}^{GJ} d\sigma/dt$ -- all as a function of t , the momentum transfer.
- Fig. 13 The differential cross section and density matrix elements for $\pi^-p \rightarrow \rho^0n$ at 15 GeV/c; the solid line is a fit to the data using the OPEA model of P. K. Williams.
- Fig. 14 The differential cross section and density matrix elements for $\pi^-p \rightarrow \rho\Delta^0$ at 15 GeV/c; the solid line is a fit to the data using the OPEA model of P. K. Williams.
- Fig. 15 The differential cross section and density matrix elements for $\pi^+p \rightarrow \rho^0\Delta^{++}$ at 15 GeV/c; the solid line is a fit to the data using the OPEA model of P. K. Williams.
- Fig. 16 The results for the $\pi^+\pi^-$ differential cross section for each 50 MeV wide $\pi^+\pi^-$ mass interval. The block points are the results of the phase shift analysis.

Fig. 17 Results of the energy independent elastic $\pi\pi$ phase shift analysis: (a) the elastic $\pi\pi$ cross section, (b) the p-wave phase shift, (c) the $I = 0$ s-wave phase shift. In (a) and (b) up and down refers to the corresponding s-wave solution. For comparison the results of Baton et al. are included in (a) and (c).

Fig. 18 Variation of χ^2 as a function of the $I = 0$ s-wave phase shift for each of the wire mass intervals.

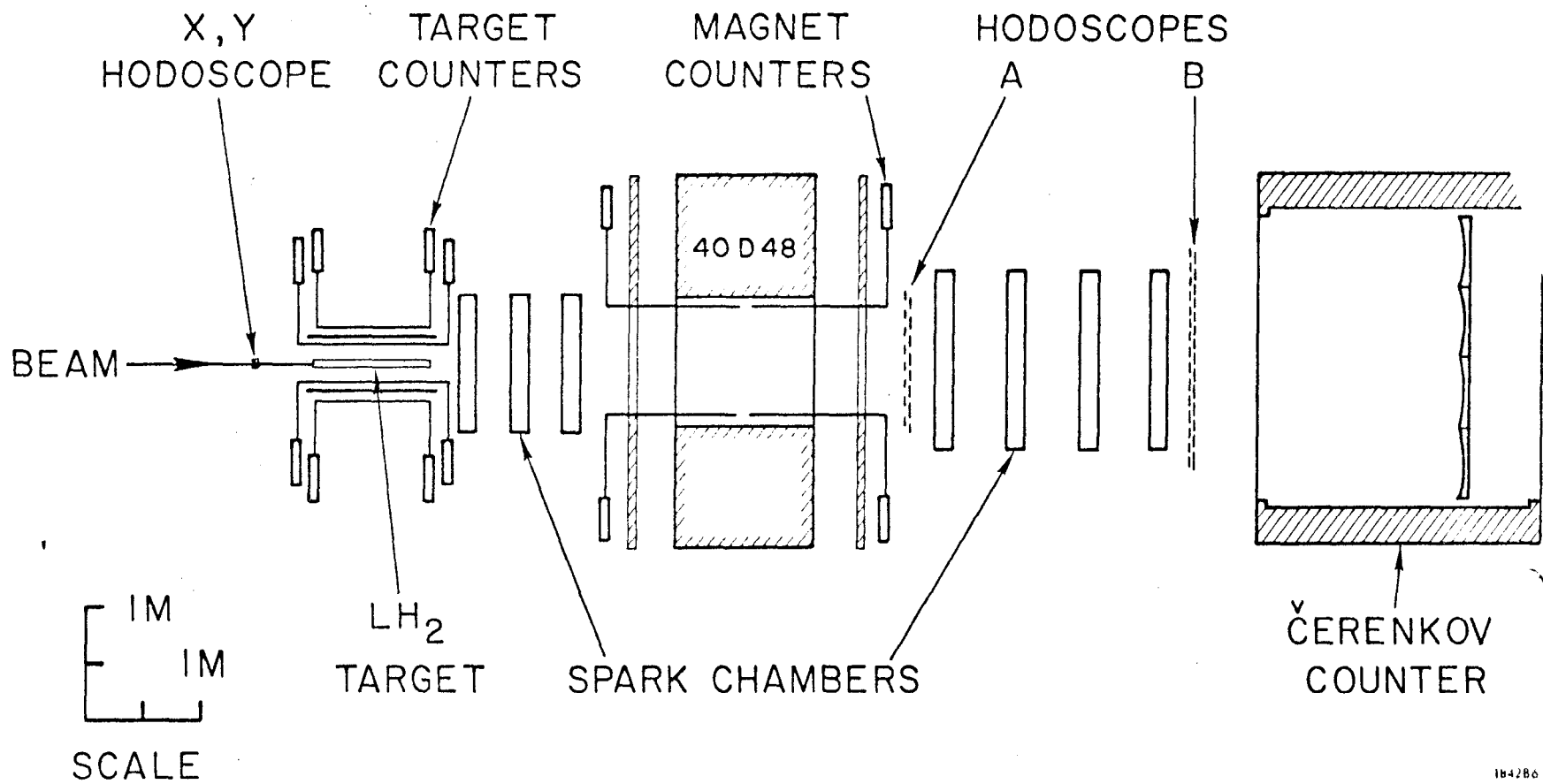


Fig. 1

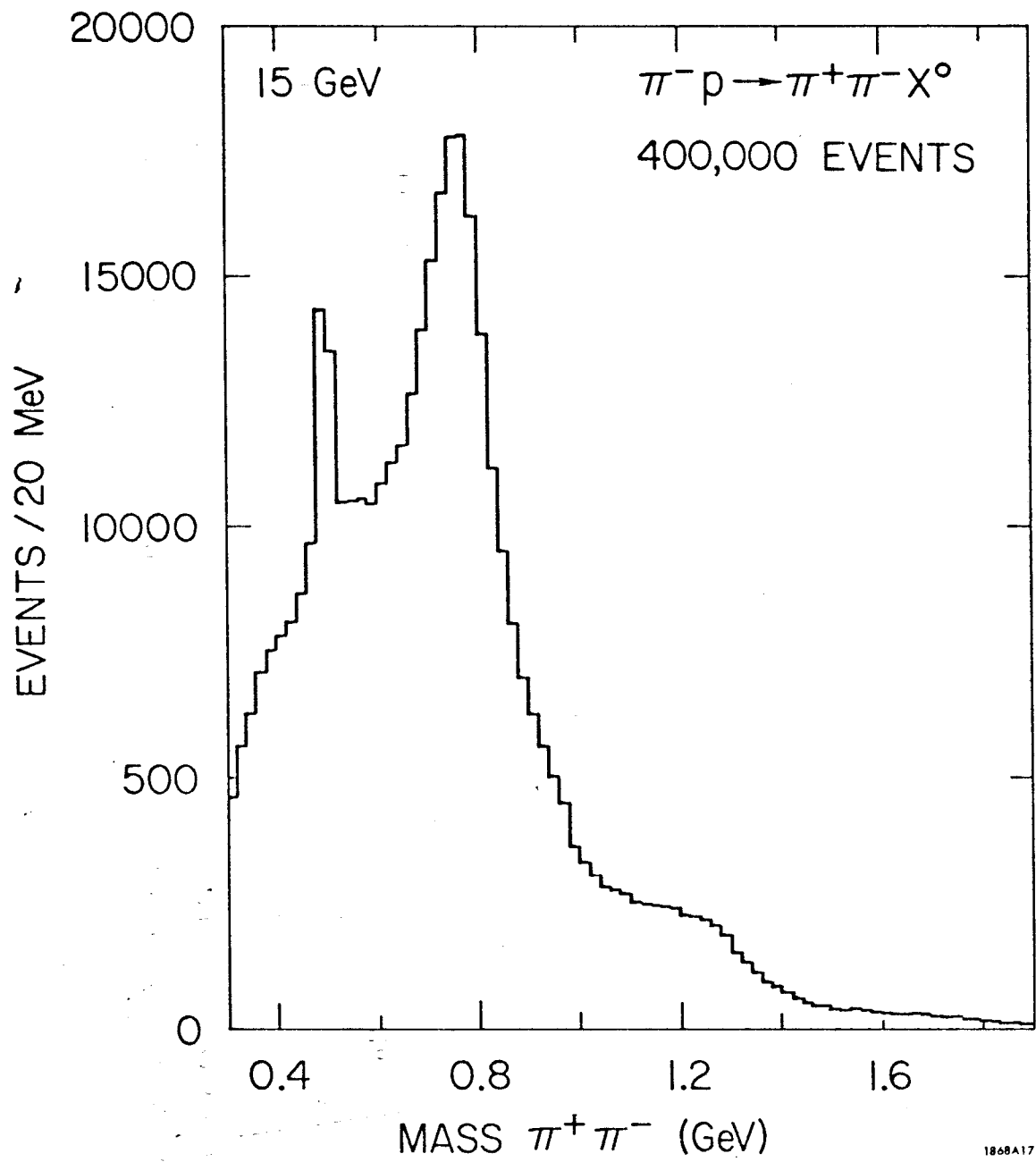


Fig. 2

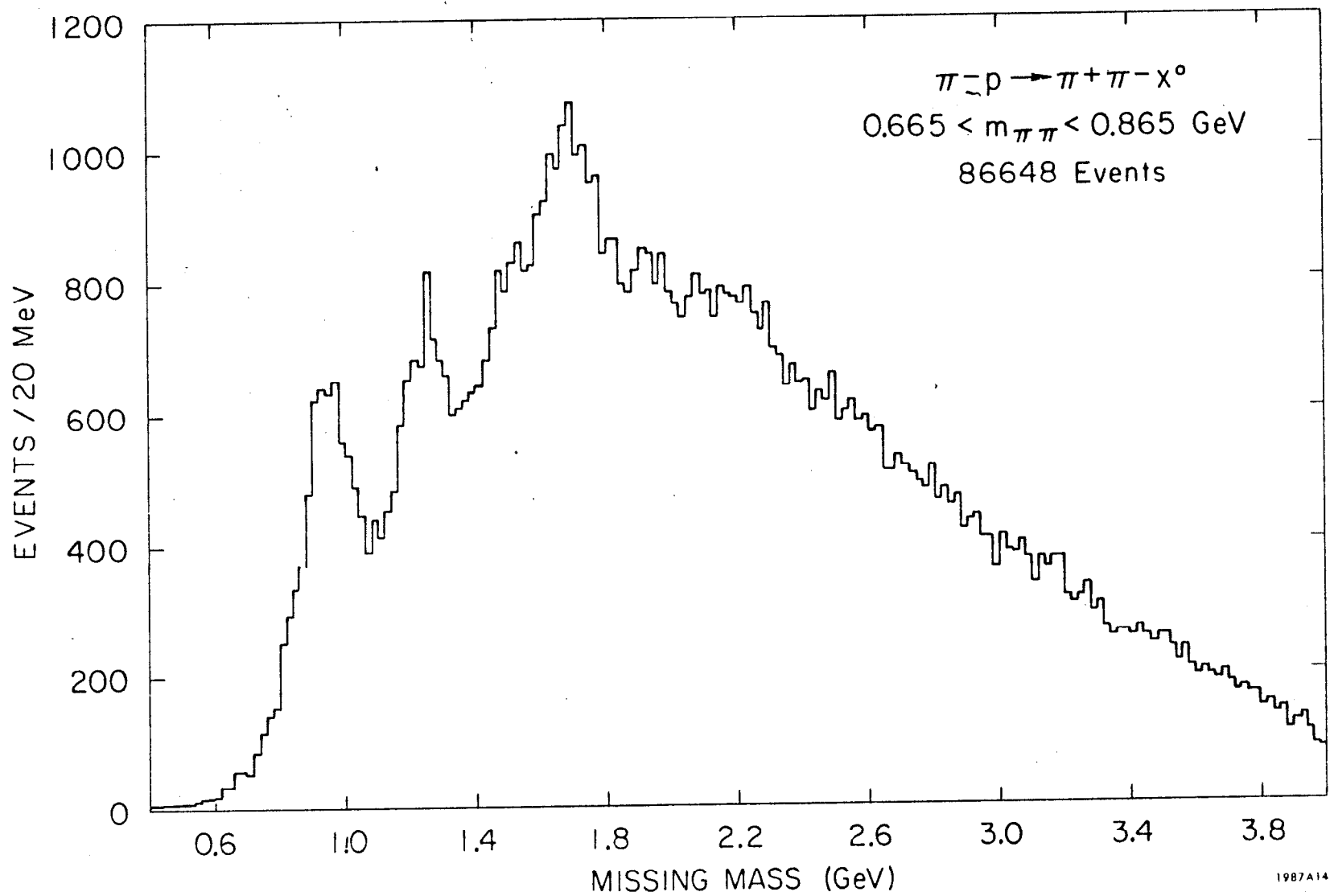


Fig. 3

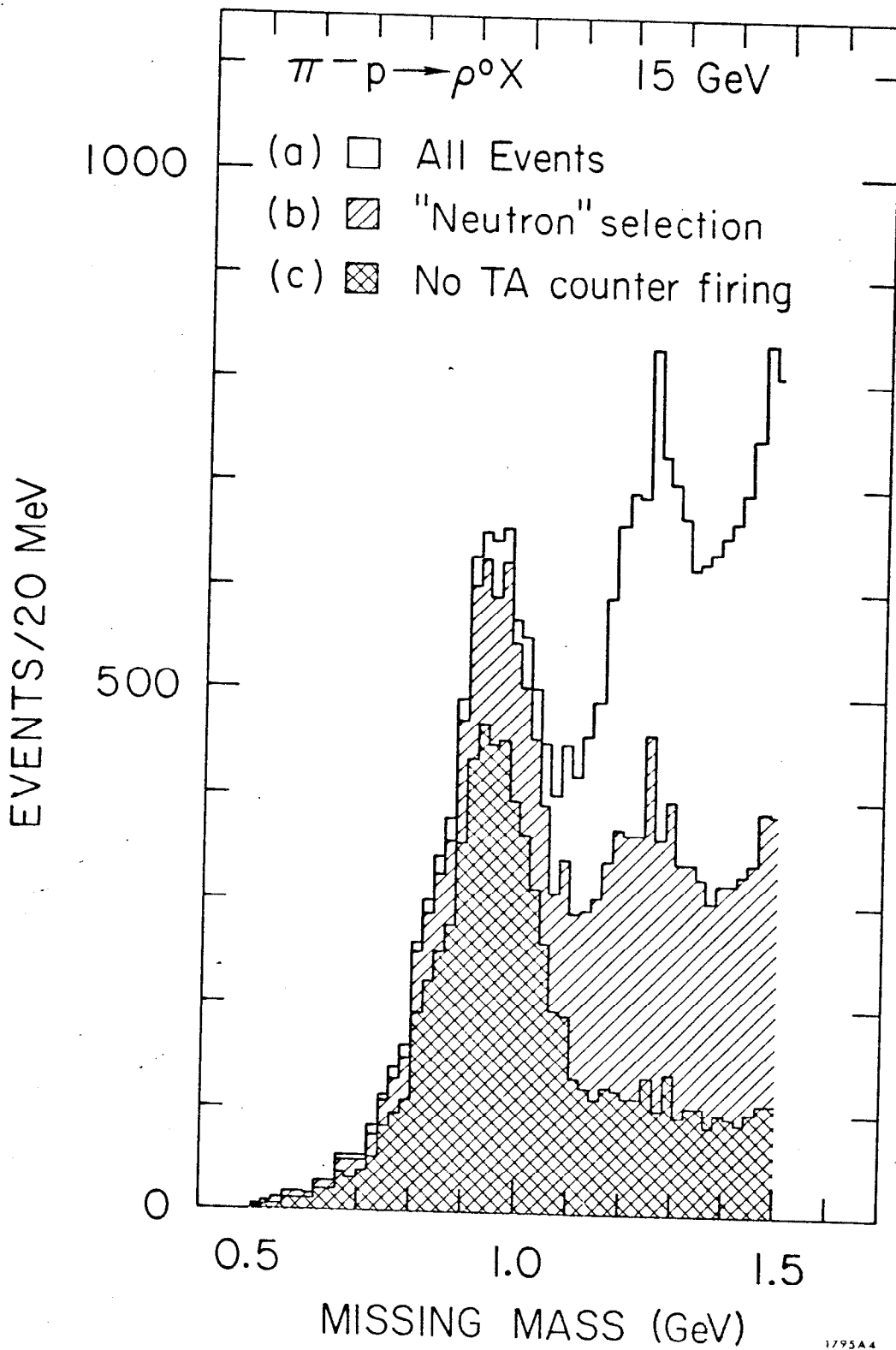


Fig. 4

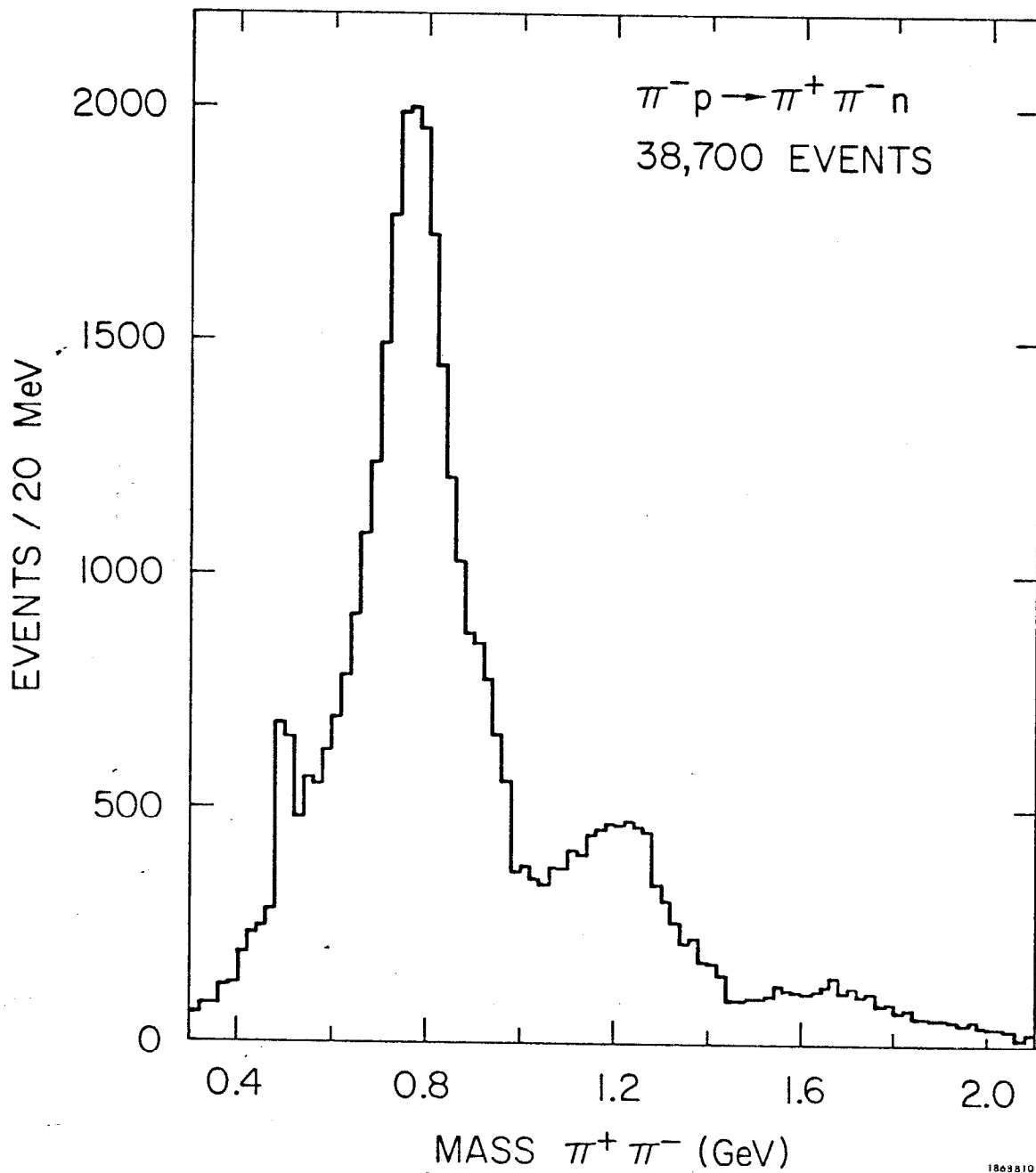


Fig. 5

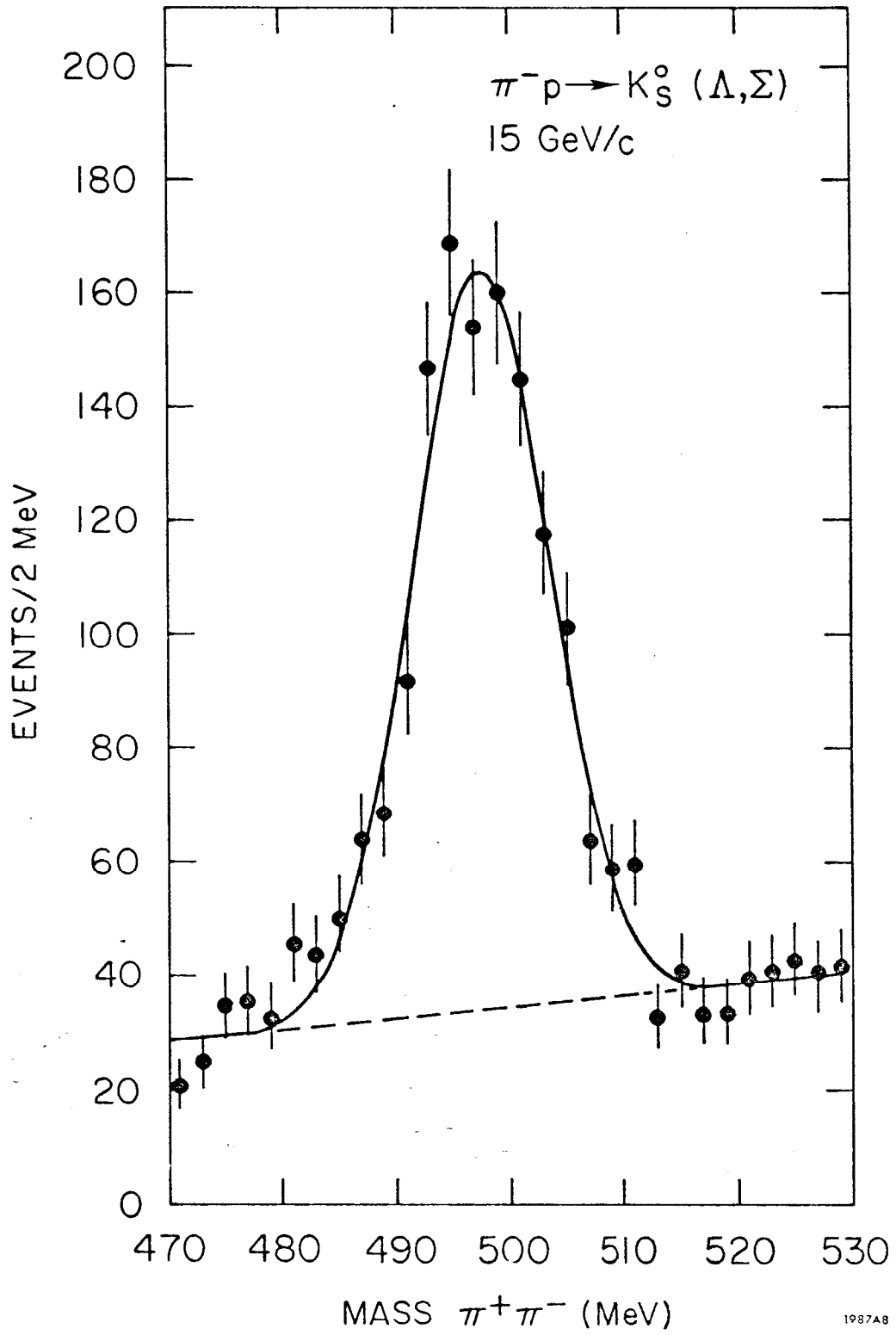


Fig. 6

$\pi^- p \rightarrow \pi^+ \pi^- n$ $0.665 < m_{\pi\pi} < 0.865$ GeV

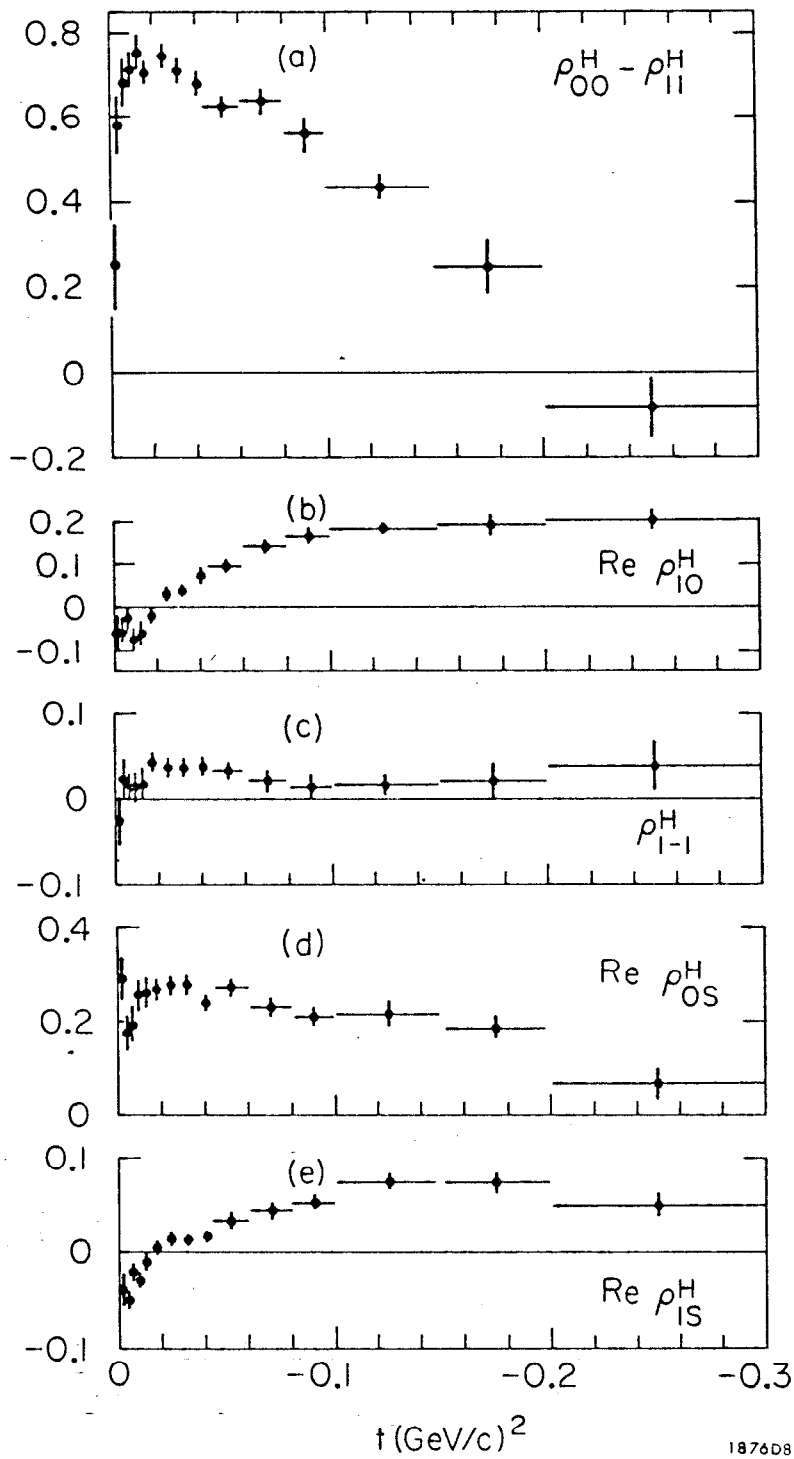


Fig. 7

$\pi^- p \rightarrow \pi^+ \pi^- n$ $0.665 < m_{\pi\pi} < 0.865$ GeV

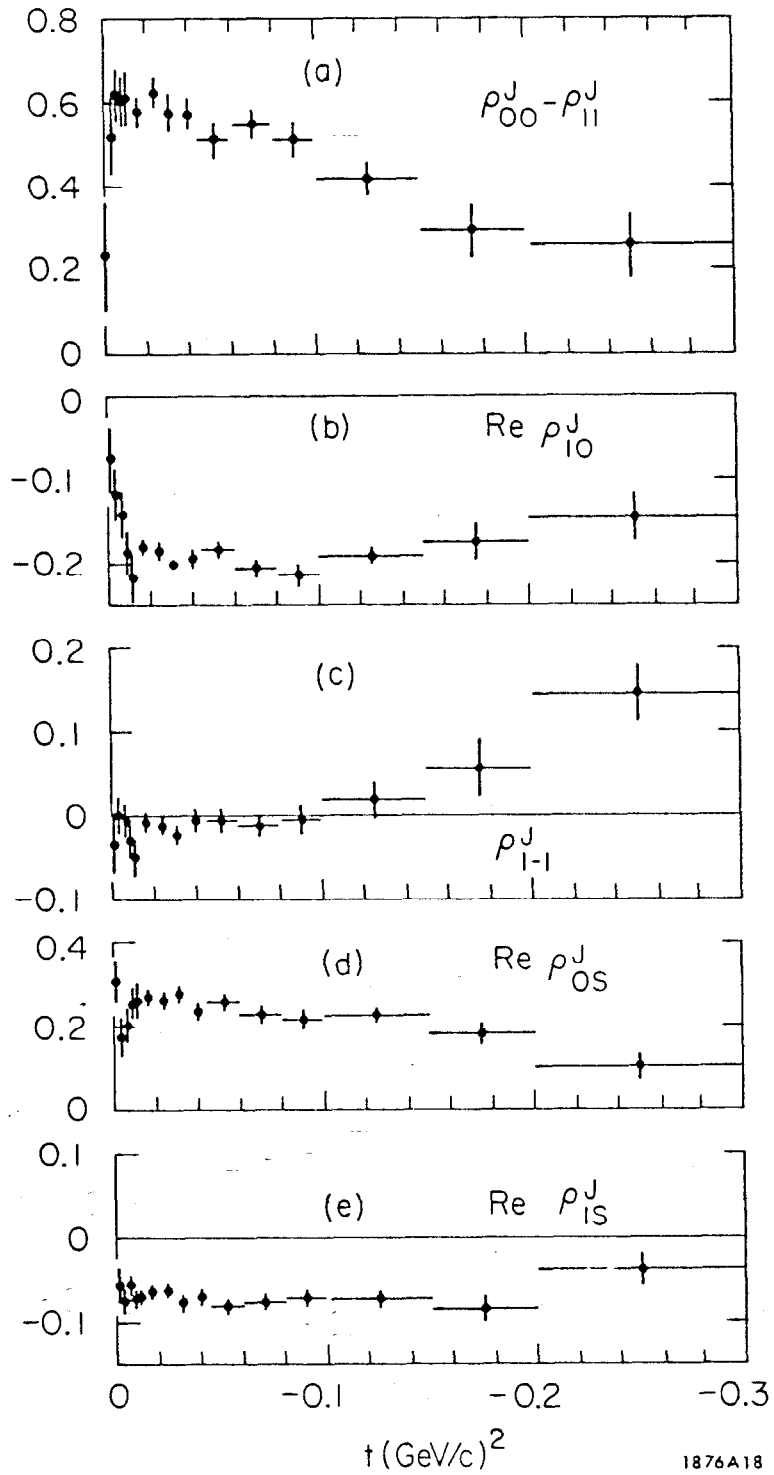
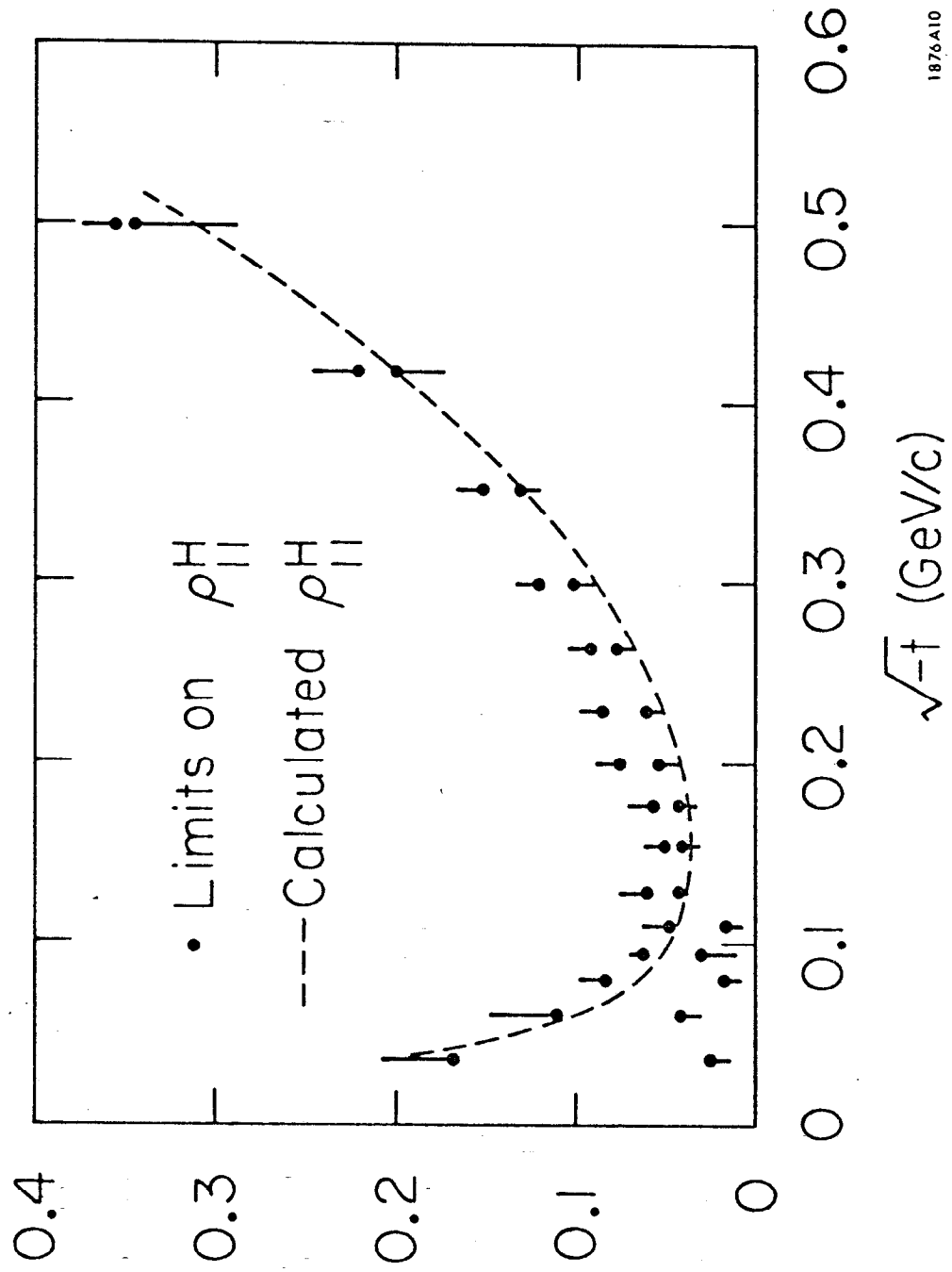
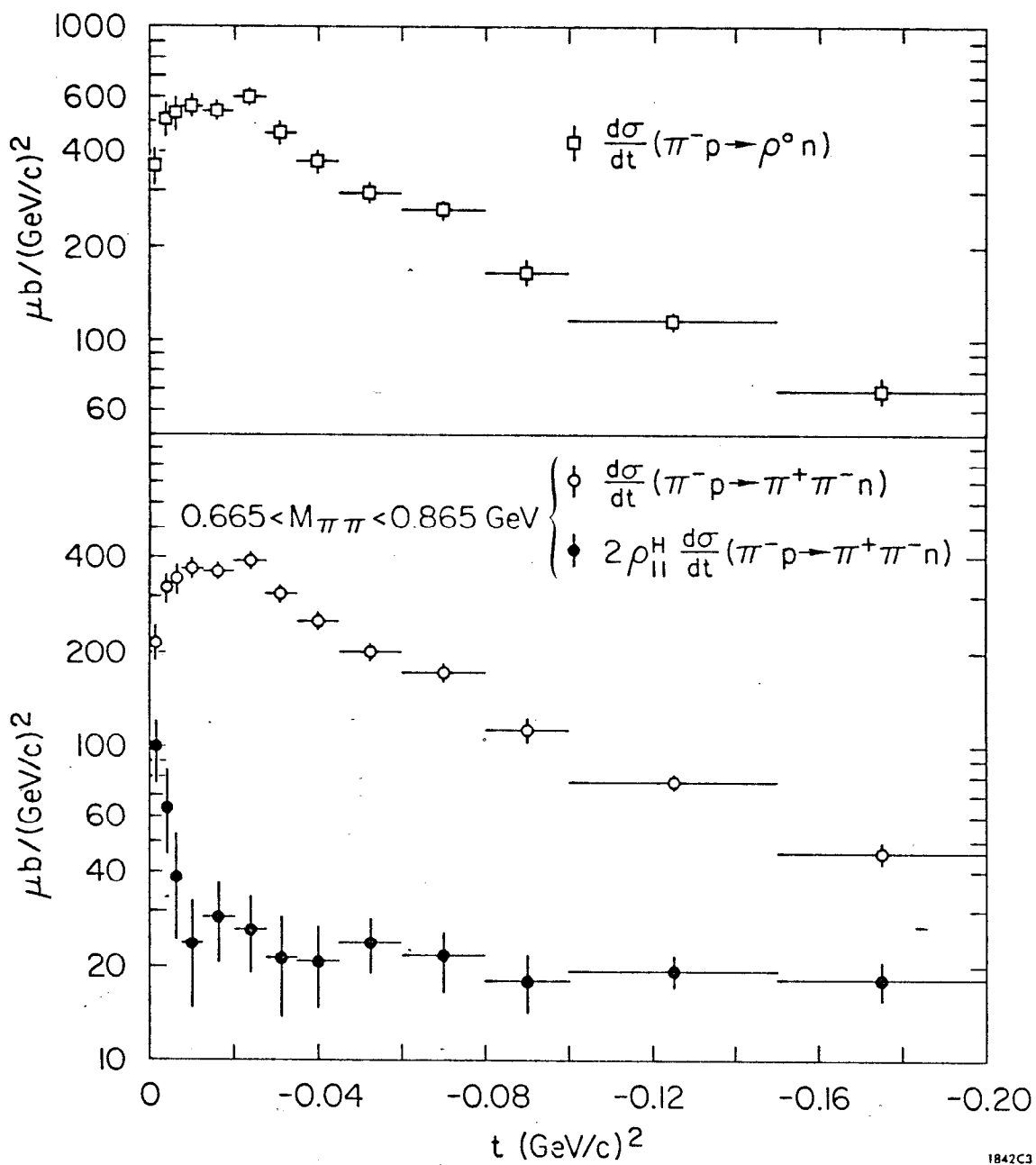


Fig. 8



1876A10

Fig. 9



1842C3

Fig. 10

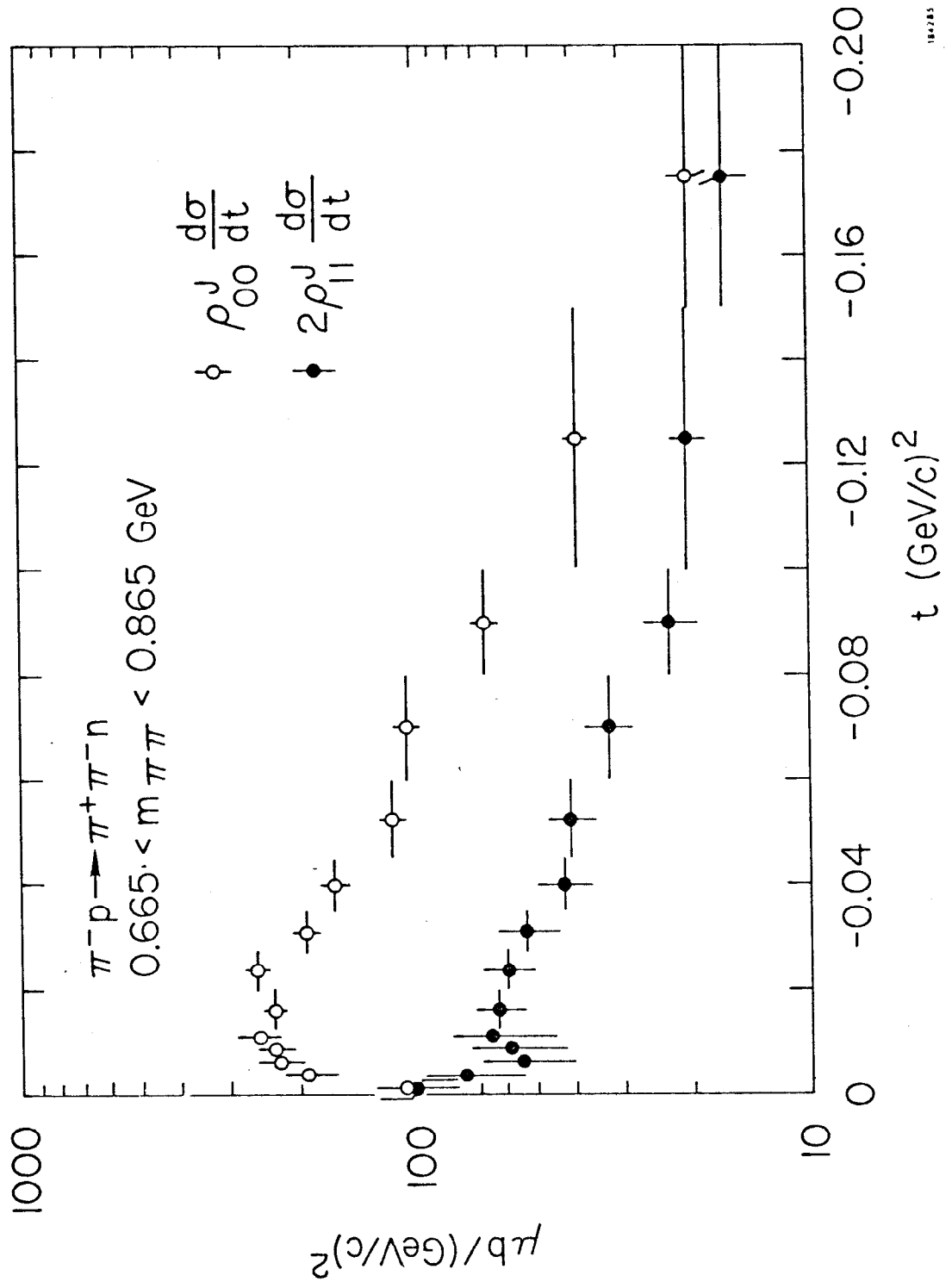


Fig. 11

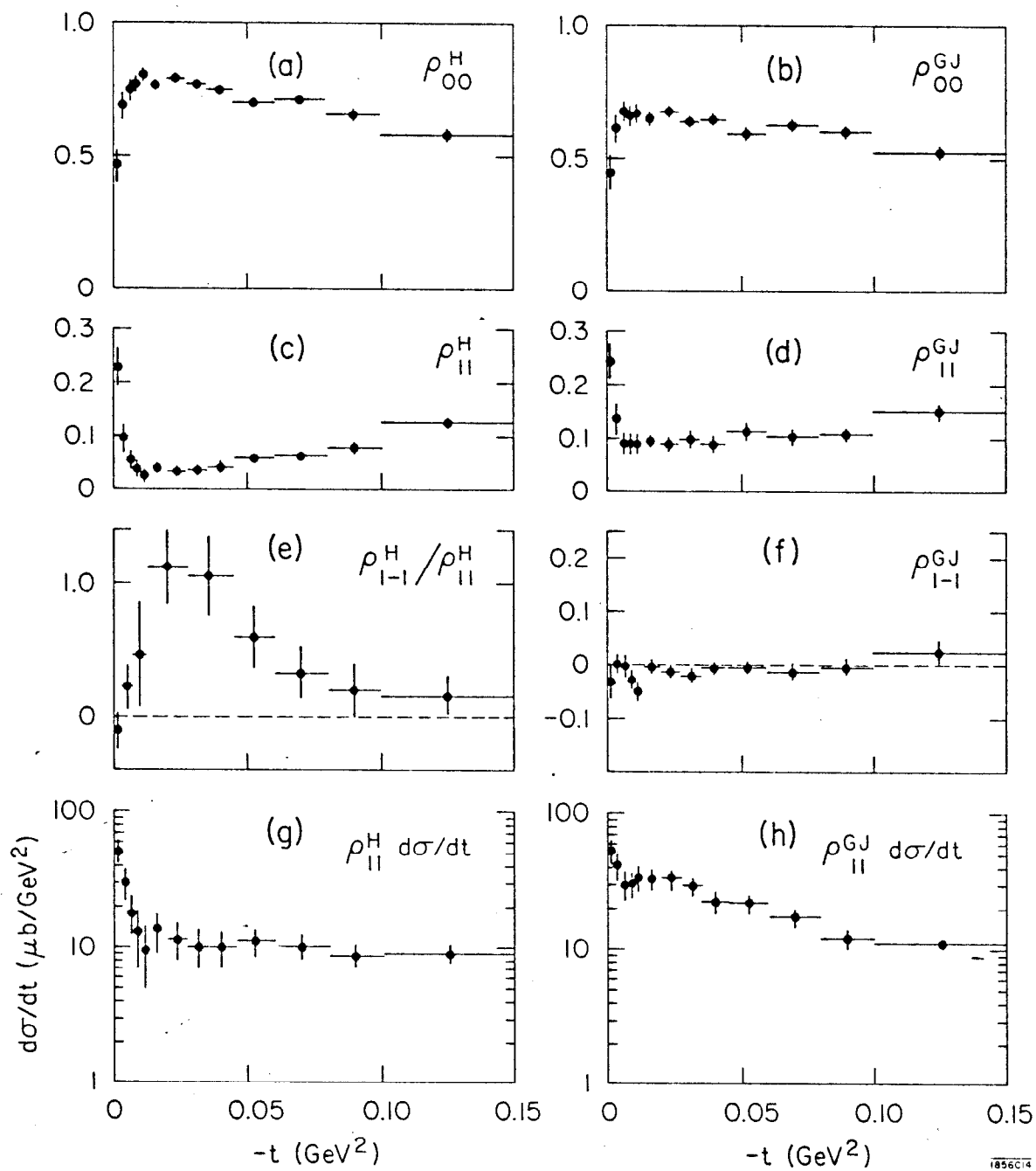


Fig. 12

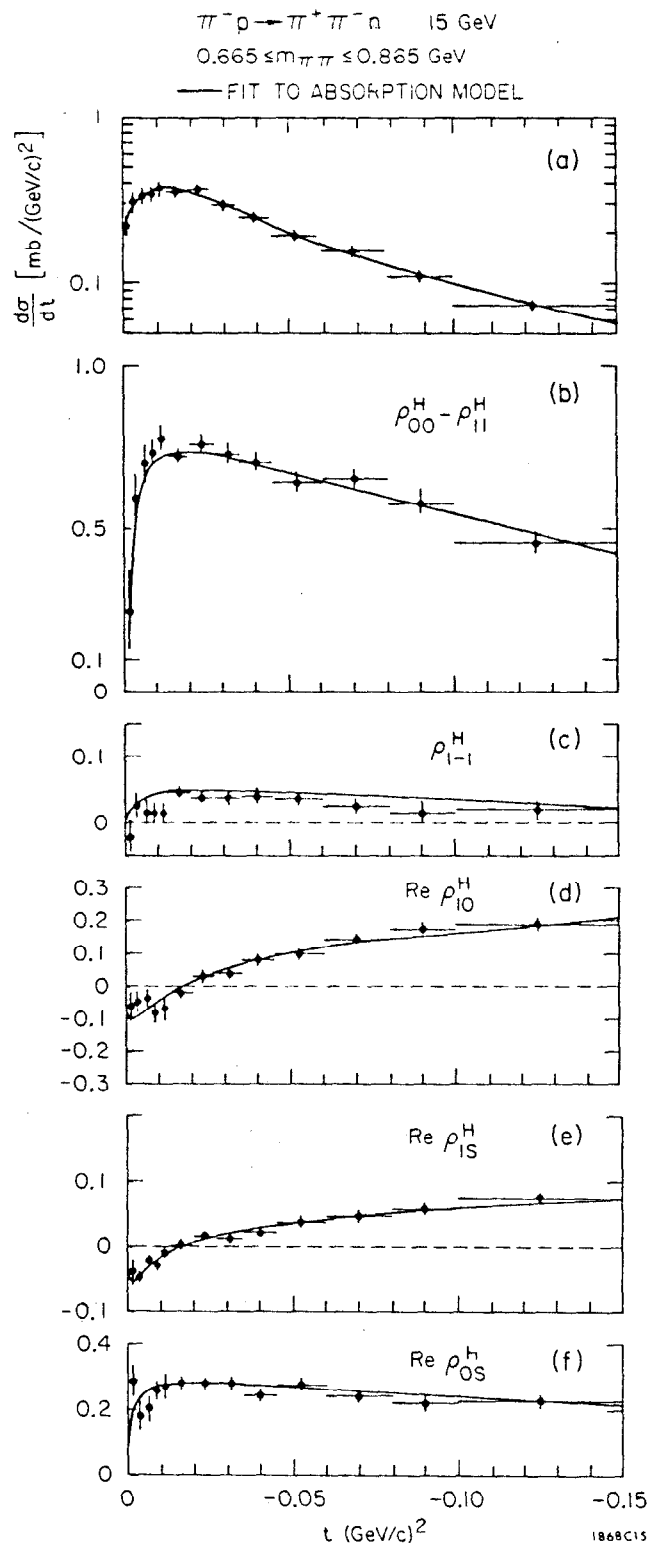


Fig. 13

$\pi^+ p \rightarrow \pi^+ \pi^- \Delta^{++}$
 $0.665 < M_{\pi\pi} < 0.865 \text{ GeV}$
 $1.04 < M_{\Delta^{++}} < 1.44 \text{ GeV}$

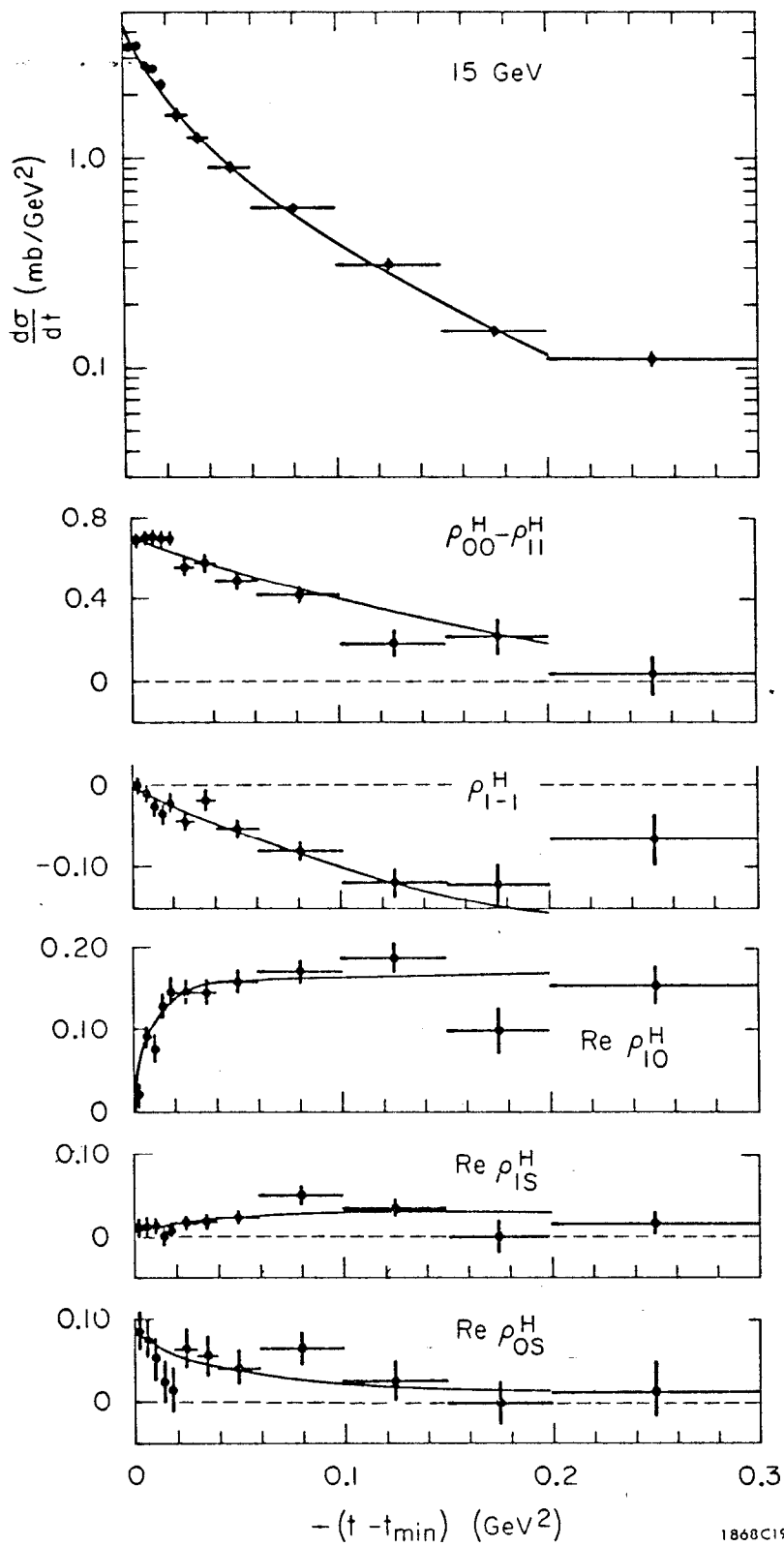


Fig. 14

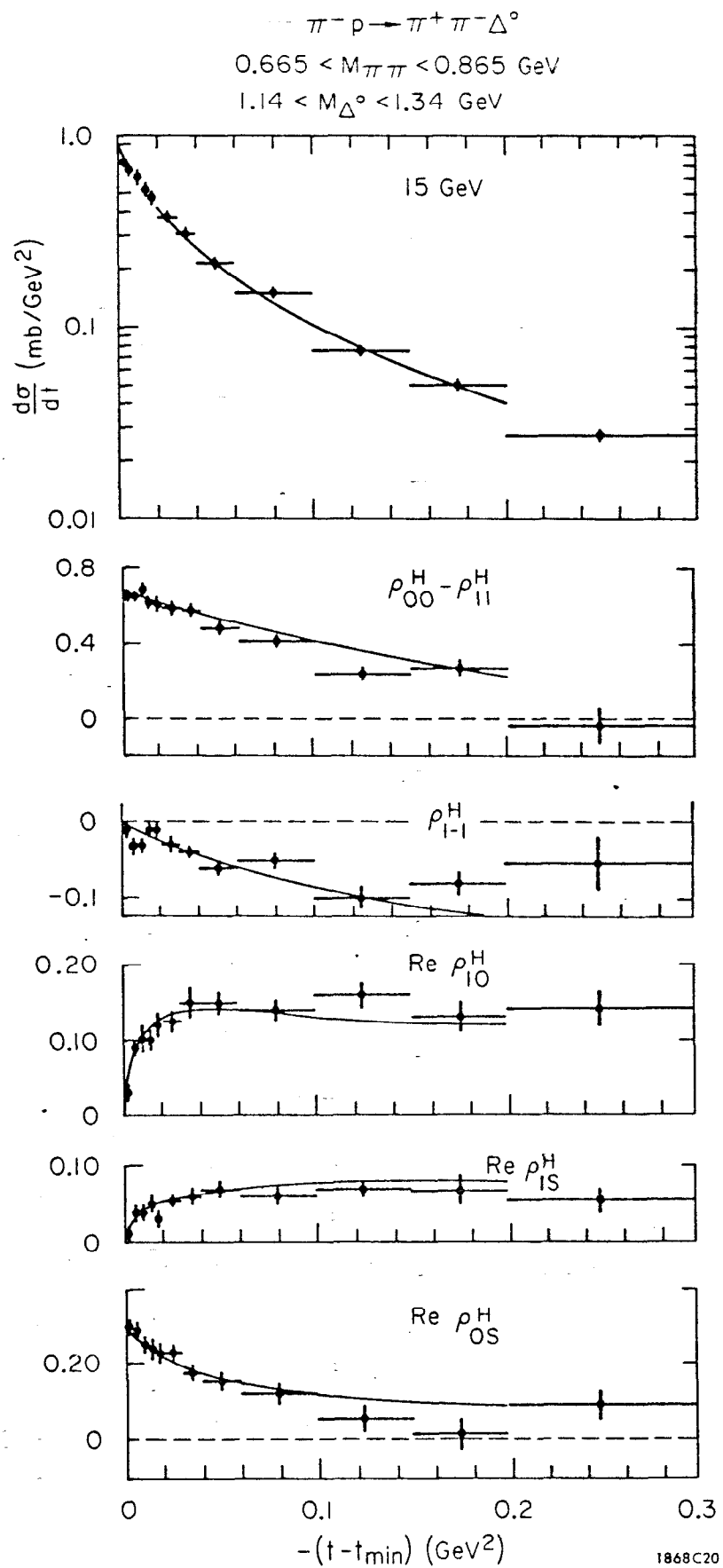


Fig. 15

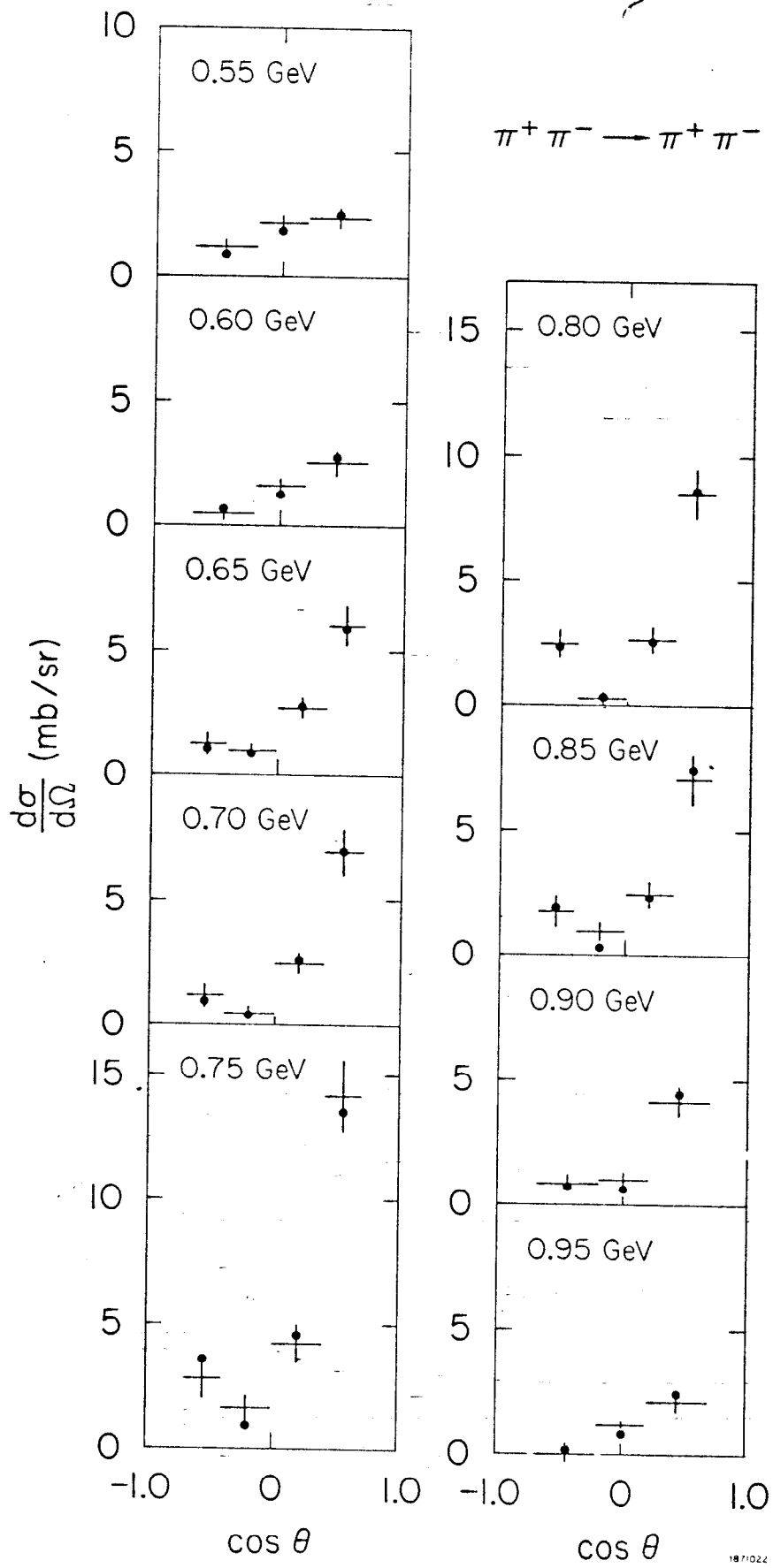


Fig. 16

1871022

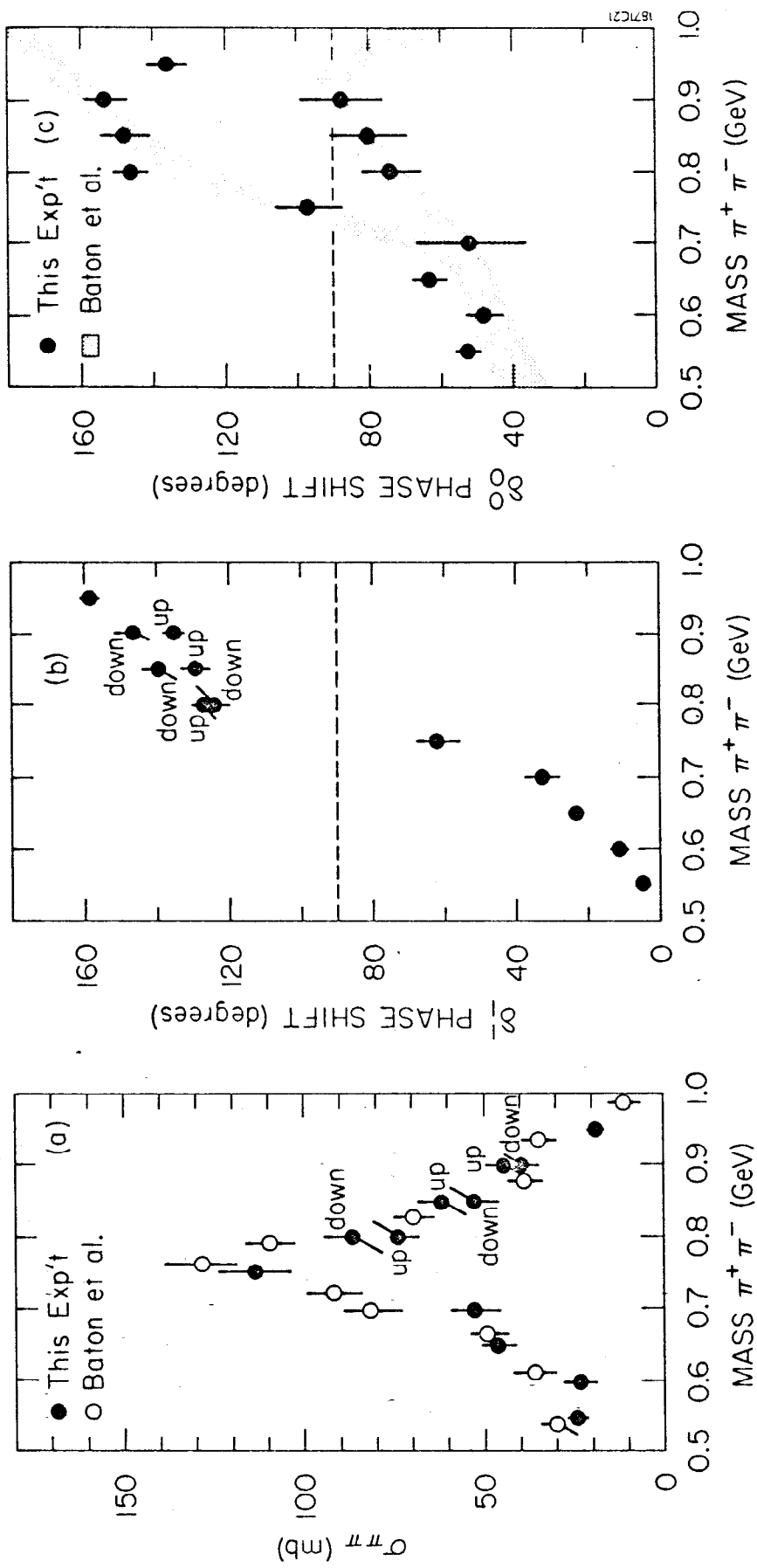


Fig. 17

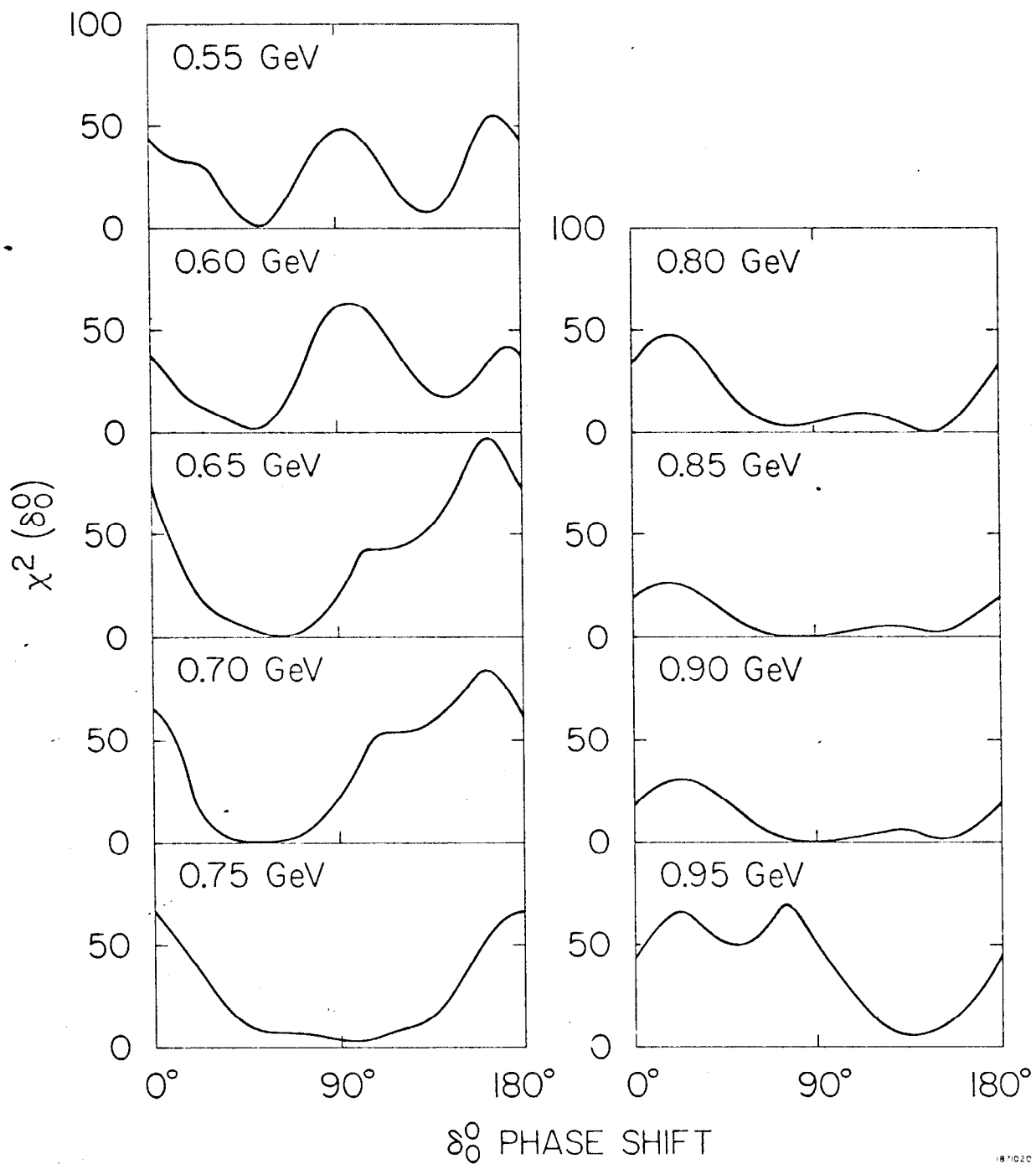


Fig. 18